Geochimica et Cosmochimica Acta 370 (2024) 89–103

Contents lists available at ScienceDirect

Geochimica et Cosmochimica Acta

journal homepage: www.elsevier.com/locate/gca

River-to-ocean pathways of beryllium-9 through estuaries

Chenyu Wang [a,*], Friedhelm von Blanckenburg [a,b], Ergang Lian [c,d], Shouye Yang [c], Jeffrey Paulo H. Perez [e], Hella Wittmann [a]

[a] GFZ German Research Centre for Geosciences, Section Earth Surface Geochemistry, Telegrafenberg, 14473 Potsdam, Germany
[b] Department of Geosciences, Freie Universität Berlin, 12249 Berlin, Germany
[c] State Key Laboratory of Marine Geology, Tongji University, 200092 Shanghai, China
[d] Research Center for Monitoring and Environmental Sciences, Taihu Basin & East China Sea Ecological Environment Supervision and Administration Authority, Ministry of Ecology and Environment, 200120 Shanghai, China
[e] GFZ German Research Centre for Geosciences, Section Interface Geochemistry, Telegrafenberg, 14473 Potsdam, Germany

ARTICLE INFO

Associate editor: Yoshiki Sohrin

Keywords:
Beryllium-9
Changjiang Estuary
Pathways
Benthic flux
Hypoxia

ABSTRACT

Estuarine processes are key in modulating the riverine input of particle-reactive trace elements to the ocean. An important, but still under-utilized member of these elements is beryllium-9 (^{9}Be) that together with cosmogenic ^{10}Be has been suggested to serve as a quantitative tracer of present and past continental weathering flux. This study investigates different pathways of terrigenous ^{9}Be through coastal areas into the ocean, based on dissolved ^{9}Be concentrations in surface and bottom waters together with corresponding particulate ^{9}Be concentrations along the salinity gradient in the Changjiang Estuary. Dissolved ^{9}Be in the Changjiang Estuary shows a non-conservative behavior: At low to mid-salinity where water is well-mixed, ^{9}Be is removed from both surface and bottom waters at low salinity and then released back into the water column at mid-salinity. At high salinity where water is stratified, dissolved ^{9}Be is removed from surface waters, but is released back into bottom waters.

In combination with hydrochemical (e.g., dissolved oxygen) and particulate ^{9}Be data obtained from different extracted phases, we attribute the removal of dissolved ^{9}Be at low salinity to salt-induced colloidal flocculation, whereas in surface waters at high salinity, we ascribe the removal to biological scavenging facilitated by phytoplankton blooms. The release of ^{9}Be into mid- and high-salinity bottom waters is likely dominated by benthic processes, including porewater diffusion and/or submarine groundwater discharge. The contribution from desorption of ^{9}Be from suspended particulate matter is negligible throughout the entire estuary. We propose that the release of ^{9}Be through benthic processes potentially presents the most important contributor to the marine ^{9}Be budget, where this benthic flux of ^{9}Be is likely enhanced by hypoxic conditions in coastal bottom waters.

1. Introduction

Estuaries play an important role in modulating riverine fluxes of trace and major elements, nutrients, and organic matter transported to the oceans (Mallick et al., 2022; Mosley and Liss, 2020; Samanta and Dalai, 2016; Yang et al., 2021). As river water mixes with seawater, changes in ionic strength, pH, concentrations of suspended particulate matter (SPM) and redox conditions alter the distribution and composition of chemical materials in the dissolved and particulate phases. Particle-reactive elements are scavenged by SPM and settle to coastal bottom sediments, from which they can be released into coastal seawater during early diagenesis (Audry et al., 2006; Homoky et al., 2016). In addition, submarine groundwater discharge may also contribute a significant quantity of dissolved elements and nutrients to the coastal ocean (Burnett et al., 2001; Kim and Kim, 2014; Moore, 1996).

The marine authigenic ^{10}Be/^{9}Be ratio is used as a proxy for, for example, deep ocean circulation patterns (von Blanckenburg et al., 1996), sea ice dynamics (Rhee et al., 2022; Sproson et al., 2022; White et al., 2019), and past continental weathering fluxes (von Blanckenburg and Bouchez, 2014; von Blanckenburg et al., 2015; Willenbring and von Blanckenburg, 2010; Wittmann et al., 2017). The ^{10}Be/^{9}Be ratio is a promising proxy for weathering flux because ^{9}Be is released from rocks by weathering. After release, ^{9}Be is partitioned into dissolved and

* Corresponding author.
E-mail address: ch_wang@gfz-potsdam.de (C. Wang).

https://doi.org/10.1016/j.gca.2024.01.029
Received 2 May 2023; Accepted 26 January 2024
Available online 9 February 2024

particulate phases and transferred to coastal oceans mainly by rivers. In the open ocean, the dissolved ^{9}Be mixes with cosmogenic ^{10}Be that is primarily sourced from the atmosphere (von Blanckenburg and Bouchez, 2014; von Blanckenburg et al., 1996). The transport pathways of ^{9}Be through estuaries to the ocean set the efficiency of ^{9}Be delivery to the oceans and in turn determine the sensitivity of the marine ^{10}Be/^{9}Be ratio as an indicator of past continental weathering. In this regard, two major pathways have been proposed by von Blanckenburg and Bouchez, (2014) and von Blanckenburg et al., (2015,2022): dissolved riverine ^{9}Be fluxes escape coastal scavenging (path 1) and reactive riverine particulate-bound ^{9}Be is released from bottom sediment into seawater (path 2). ^{9}Be input via path 1 is assumed to be proportional to the continental ^{9}Be weathering flux if the extent of coastal scavenging remains unchanged (von Blanckenburg and Bouchez, 2014), whereas path 2 is suggested to depend primarily on sediment delivery flux and the rate of benthic release processes, but to be independent of coastal scavenging (von Blanckenburg et al., 2015).

Recently, the validity of these assumptions was questioned. Li et al. (2021) contend that coastal scavenging could be enhanced when sediment influx, resulting from increased denudation rate, is high. This, in turn, may counterbalance the increased dissolved ^{9}Be flux through path 1, thus rendering marine ^{10}Be/^{9}Be ratio insensitive to weathering flux. However, their model does not take into account that river particle concentration and denudation rate are not linearly correlated (Milliman and Farnsworth, 2011), and further ignores the particulate ^{9}Be source (von Blanckenburg and Bouchez, 2014; von Blanckenburg et al., 2022). A recent study based on porewater Be data suggested that diagenetic release of ^{9}Be from coastal sediments (path 2) could be the dominating oceanic ^{9}Be input flux (Deng et al., 2023). Given these debates, clarifying the pathways of terrigenous ^{9}Be into the ocean through estuaries and their relative significance is thus fundamental towards interpreting marine ^{10}Be/^{9}Be records.

So far, studies on ^{9}Be behavior in estuaries have covered seven estuaries (Brown et al., 1992; Kong et al., 2021; Kusakabe et al., 1991; Measures and Edmond, 1983; Suhrhoff et al., 2019), and most of them focused on dissolved ^{9}Be in surface waters. The behavior of dissolved ^{9}Be documented in these estuaries appears to be highly variable. While dissolved ^{9}Be in the Amazon and Congo river estuaries is removed from surface waters (Brown et al., 1992; Measures and Edmond, 1983), the Ganges, Changjiang (Yangtze River), Pearl River and Zrmanja estuaries are characterized by the release of ^{9}Be from particulates (Brown et al., 1992; Kusakabe et al., 1991; Measures and Edmond, 1983; Suhrhoff et al., 2019). A small estuary in Scotland, Loch Etive, however displays nearly conservative mixing behavior (Suhrhoff et al., 2019), meaning the decrease of dissolved ^{9}Be concentrations along a predictable vector that results from river - ocean water mixing. The variable behavior of dissolved ^{9}Be in different estuaries implies a high sensitivity of ^{9}Be to hydrochemistry (e.g., colloidal load and composition, Suhrhoff et al., 2019) and estuarine processes. Understanding the behavior of dissolved ^{9}Be under different hydro-physicochemical conditions is thus important for clarifying the different pathways of terrigenous ^{9}Be into the ocean.

In this study, we report dissolved ^{9}Be concentrations in both surface and bottom waters along the entire salinity gradient in the Changjiang Estuary, together with the particulate ^{9}Be concentrations in different chemically extractable fractions of the corresponding SPM. In a previous study low-resolution dissolved ^{9}Be data of Changjiang Estuary surface waters were reported (Measures and Edmond, 1983). The Changjiang River is historically the fourth largest rivers of the world in terms of sediment discharge before the impoundment of the Three Gorges Dam (TGD) (Milliman and Farnsworth, 2011). Its estuary represents a typical large, river-dominated estuary characterized by complex hydrodynamic processes that generate a seasonal turbidity-maximum zones (TMZ) and hypoxic conditions (Lin et al., 2020; Zhu et al., 2016; Diaz and Rosenberg, 2008). Because these are globally common phenomena, the Changjiang Estuary serves as a natural laboratory where the different pathways of ^{9}Be into the ocean under a variety of hydro-physicochemical estuarine conditions can be explored.

2. Study area, materials and methods

2.1. The Changjiang River and its estuary

The Changjiang River is the third longest river in the world, flowing 6300 km eastwards from the Tibetan Plateau into the East China Sea. It historically delivered ~900 km^3/yr of water and ~470 Mt/yr of sediment into the Changjiang Estuary and the adjacent sea (Milliman and Farnsworth, 2011). The Changjiang watershed is mainly overlain by sedimentary rocks composed of marine carbonates, evaporites and alluvium from Precambrian to Quaternary in age. The river water chemistry is dominated by limestone weathering, leading to neutral or slightly alkaline water pH (Chetelat et al., 2008).

The Changjiang Estuary is a mesotidal, partially mixed estuary, with a tide of regular semidiurnal type. The general circulation pattern in the Changjiang Estuary and the adjacent East China sea (ECS) in summer is shown in Fig. 1. The Changjiang River enters the East China Sea, forming the highly dynamic Changjiang Diluted Water (CDW) system. The Taiwan Warm Current (TWC) flows northeastward parallel to the 50-m isobath and enters the submerged river valley off the Changjiang, which can be further divided into the Taiwan Warm Current Surface Water (TWCSW) and Taiwan Warm Current Deep Water (TWCDW) (Zhang et al., 2014). In summer, the TWCSW originates mostly from the Taiwan Strait Warm Current, while the Kuroshio Subsurface Water dominates the TWCDW (Lian et al., 2016; Zhang et al., 2014).

From the complex and dynamic interactions between runoff, stratification and tides (Li and Zhang, 1998; Wu et al., 2012), a turbidity maximum zone develops in the river mouth zone of the Changjiang Estuary where the bottom SPM concentration can be >10 g/L (Lin et al., 2020). The deposition of abundant riverine SPM causes the upstream Changjiang Estuary to be very shallow (6.5 m average) (Wang and Liu, 2003). The Changjiang Estuary water is dominated by oxic conditions, with occasional occurrence of seasonal hypoxia. Hypoxic conditions usually occur below the pycnocline in summer, reaching a maximum in August, then weaken in autumn, and finally disappear in winter (Zhu et al., 2016).

2.2. Sample collection

Field sampling was conducted between August and September 2019 during the cruise of the Key Elements Cycling in the Changjiang-Estuary-Shelf Transect (KECES 2019) organized by the State Key Laboratory of Marine Geology, Tongji University. A total of 15 stations (located between 120°-126°E and 29°–32°N, Fig. 1) were sampled along the Changjiang-Estuary-Shelf Transect from the river mouth of Changjiang (sampling station C1, 121.06°E, 31.78°N) to the East China Sea continental shelf (station C18, 124.99°E, 29.86°N). Surface seawater samples were collected approximately 3–4 m upstream from the ship's bow via a pre-cleaned Masterflex I/P® Precision Pump tubing (C-Flex®) attached to the front end of a carbon fibre pole sampler, and water was pumped by a peristaltic pump. Near-bottom (~2 m above the seafloor) water samples were collected using a 5 L Teflon-coated Niskin-X bottle attached to a nylon rope. After collection, samples were immediately filtered onboard through an acid-cleaned 0.45 μm filter (147 mm in diameter, Supor® PES, Pall) using a customized Teflon filter holder. The filtrates were stored in pre-cleaned LDPE bottles (Nalgene), acidified to pH < 2 with trace metal grade HCl, and stored at 4 °C until ^{9}Be analysis. After filtering, the membranes (trapping SPM) were also stored refrigerated at 4 °C. The SPM samples were dried to constant weight at 40 °C in a hot-air convection oven over several days upon arrival in the laboratory.

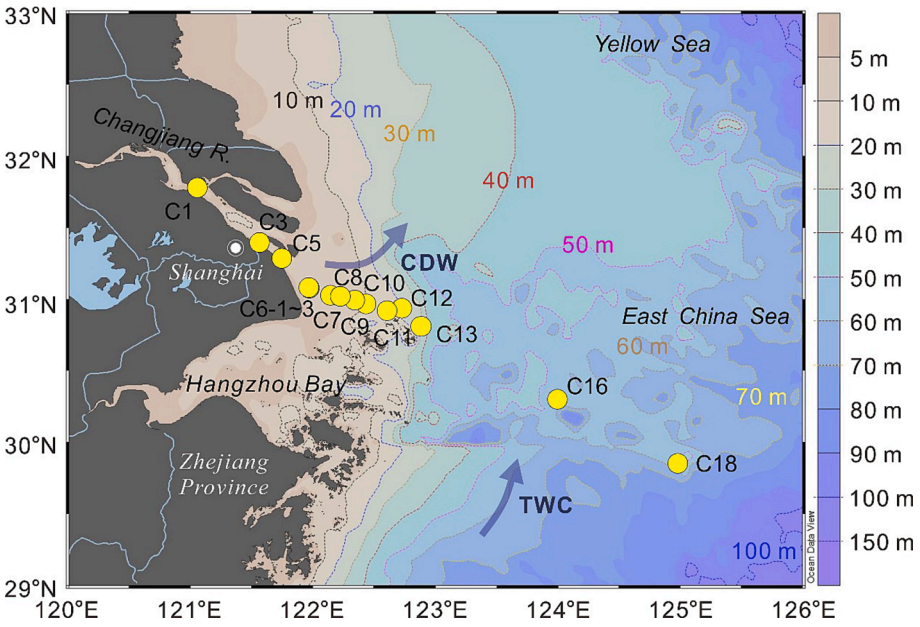

Fig. 1. Map showing the locations of sampling stations along the Changjiang-Estuary-Shelf Transect. Major water masses in the study area in summer are indicated: CDW, Changjiang Diluted Water; TWC, Taiwan Warm Current. All maps in this article were created using "Ocean Data View" (https://odv.awi.de, 2022.).

2.3. Analytical methods

2.3.1. Auxiliary parameters

Salinity, temperature and dissolved oxygen (DO) were recorded with a SBE25 Conductivity-Temperature-Depth (CTD) recorder (Sea-Bird) equipped with a SBE43 DO sensor. The salinity was calibrated by the salinity of discrete samples measured by a Multi 340i multi-parameter meter (WTW), and the DO sensor was calibrated against water sample analyses conducted by the Winkler titration method (Carpenter, 1965). The pH was determined using a pH-meter (PHS-3C), with analytical uncertainty of 0.01 units. The SPM concentration was determined by weighting the difference of dried membranes (pre-cleaned in 0.1 M HCl) before and after water filtration of a given volume of water.

2.3.2. Dissolved ^{9}Be analysis

^{9}Be was preconcentrated from 100 to 200 mL of seawater using the iron co-precipitation method following established protocols (Wang et al., 2024). After preconcentration, the samples were dissolved in 1 mL 3 % HNO_3 doped with 1 ng/g rhodium (Rh) as internal standard to correct machine drift for ^{9}Be analysis on a sector-field high-resolution inductively coupled plasma-mass spectrometer (HR-ICP-MS, Element2, Thermo Fisher Scientific) in low-resolution mode. The doubly charged ion rate was less than 3 % and the oxide formation rate was less than 5 %. ^{9}Be was quantified by an external calibration with standards prepared gravimetrically from our in-house ^{9}Be carrier solution. All the measurements were carried out at the Helmholtz Laboratory for the Geochemistry of the Earth Surface at GFZ Potsdam, Germany (von Blanckenburg et al., 2016). Procedure blanks were always below the detection limit (average instrument blank plus 3 times standard deviation (SD); as low as 4.0 pg Be, at most 15.0 pg Be), which accounts for 3–21 % of ^{9}Be in our samples. Final Be concentrations were thus not corrected for procedural blanks. The long-term external precision was 5 % (1SD, n = 14), monitored by processing an in-house artificial seawater standard (prepared by synthetic salt, Dupla Marin Premium Reef Salt Natural Balance, product code DM81432_MA) from January 2021 to January 2022. Since no certified seawater standard is available for ^{9}Be, we spiked artificial seawater (100–200 mL) with known amounts of ^{9}Be (from 5 pg/g to 20 pg/g) to monitor accuracy. The calculated ^{9}Be yields were within ±10 %, with an average of 97.6 ± 5.6 % (1SD, n = 13). Hence, we propagated a relative uncertainty of 10 % to all ^{9}Be measurements as a conservative estimate.

2.3.3. Particulate ^{9}Be and elemental concentration analyses from sequential extraction

We applied Be-extraction procedures to SPM samples to analyze ^{9}Be and other element concentrations in the extracted and the remaining silicate residue fractions, with the aim to investigate the possible redistribution of ^{9}Be between the dissolved phase and extractable phases of SPM. About 0.5 to 1 g of SPM was washed 3 times using pH 8-adjusted Milli-Q water in order to remove the remaining sea salt. After that, four fractions were sequentially extracted following the modified procedure from Wittmann et al. (2012), including: 1) the exchangeable fraction ("ex", 1 M CH_3COONH_4) containing weakly adsorbed elements retained on the SPM surface by relatively weak electrostatic interactions, 2) the reactive oxy-hydroxide fraction ("reac", 0.5 M HCl, 1 M NH_4OHxHCl) containing amorphous and crystalline (hydr)oxides, note that this treatment would also dissolve carbonate phases present in the sample, 3) the organic fraction ("org", 0.01 M HNO_3, 10 M H_2O_2) containing the organic matter, and 4) the remaining silicate residue fraction ("min", 28 M HF, 14 M HNO_3) containing the lithogenic crystalline minerals.

To extract the exchangeable fraction, 12 mL of 1 M ammonium acetate (pH = 7) (Óvári et al., 2001) was added to each sample in precleaned centrifuge tubes. The tube was placed on a reciprocating shaker for 24 h to achieve equilibrium with respect to Be sorption. After equilibration, the slurry was centrifuged at 4000 rpm and the supernatant was decanted. The residue was washed twice with Milli-Q water and the wash solutions were collected along with the supernatant. Except for the exchangeable fraction, reagents used for the other fractions and the detailed procedures can be found in Wittmann et al. (2012). The exchangeable fraction leachate was further purified using the iron co-precipitation method for ^{9}Be determination on the HR-ICP-MS, following the same protocol applied to seawater samples. ^{9}Be analyses for the other fractions as well as other elemental analyses were performed using an optical emission, inductively-coupled plasma spectrometer (ICP-OES, model Varian 720-ES with axial optics). The long-term external uncertainty for OES measurement is 5 % (1SD) (Wittmann et al., 2012).

2.3.4. Specific surface area (SSA) and powder X-ray diffraction (XRD) analyses

The specific surface area (SSA) was calculated using the Brunauer–Emmett–Teller (BET) equation (Brunauer et al., 1938). Prior to N_2 sorption measurements, samples were vacuum-dried at room temperature for at least 16 h, followed by degassing under heating and vacuum, using a VacPrepTM 061 Sample Degas System (Micromeritics, Norcross, GA, USA) The accuracy and precision of the SSA measurement is ~1.1 % and 0.29 %, respectively, based on repeat analysis (n = 3) of Micromeritics certified reference material (Carbon Black, 044–16833-00, $SSA_{BET} = 21.52 \pm 0.75\ m^2\ g^{-1}$).

The mineralogical composition of the SPM samples was identified by powder X-ray diffraction (XRD) analysis. XRD measurements were performed using a STOE STADI P diffractometer with a Cu X-ray source fitted with a curved Ge (1 1 1) monochromator and a DECTRIS MYTHEN2 detector in a flat plate transmission geometry. Diffraction patterns were measured over the 2θ range of 0–84°, with the sample plate being rotated relative to 2θ at a ratio of 1:2 and a data collection time of about 7 min per data point with a resolution of 0.015° 2θ. All the measurements were carried out in the Mineral Synthesis and Characterization Laboratories at GFZ Potsdam.

3. Results

3.1. Water physicochemical properties

Water physicochemical properties of the studied 15 stations along the Changjiang-Estuary-Shelf Transect are shown in Fig. 2 and Table 1. In general, water was vertically well-mixed at salinities (S) below 20 PSU (practical salinity units, in permill), but stratified when S > 20 PSU, as indicated by the vertical distribution of salinity and temperature (Fig. 2a and b). We thus divided the transect into a well-mixed zone (low-mid salinity, S ≤ 20 PSU, stations C1-C9) and a stratified zone (high salinity, S > 20 PSU, C10-C18). In the well-mixed zone, the water was well-oxygenated (DO > 5 mg/L) with a nearly constant pH value ranging from 7.8 to 7.9 (Fig. 2c and d). A turbidity maximum zone occurred over a salinity range of 6–18 PSU where water depths are shallower (Fig. 2c and e, from station C6-2 to C9), and taking 0.7 g/L as the threshold value of the turbidity maximum zone (Jiang et al., 2013). The SPM concentrations were generally higher in bottom waters (average of 0.83 g/L) than in surface waters (average of 0.39 g/L) (Table 1). In the stratified zone, the pH value of surface waters (average of 8.14) is slightly higher than that of bottom waters (average of 7.82). The DO progressively decreased from surface to bottom waters, reaching hypoxic levels (threshold of 2 mg O_2/L, Vaquer-Sunyer and Duarte (2008)) near the bottom of station C13. Although the SPM concentrations do not vary as significantly as in the well-mixed zone, they were still higher in the bottom (average of 0.11 g/L) than in surface waters (average of 0.02 g/L) (Table 1).

3.2. Dissolved ^9Be

Dissolved ^9Be concentrations ($[^9Be]_{diss}$, square brackets denote concentrations) along the Changjiang-Estuary-Shelf Transect varied from 0.02 nM to 0.15 nM (Table 1, Fig. 3), comparable to previously published data (Measures and Edmond, 1983). The $[^9Be]_{diss}$ in surface and bottom waters are nearly identical at S ≤ 20 PSU, but diverge at > 20 PSU. This characteristic corresponds to the stratification of water (section 3.1). In the well-mixed zone (S < 20 PSU), $[^9Be]_{diss}$ in both surface and bottom waters decrease during the initial mixing between river water and seawater, reaching a minimum at about S = 4 PSU. After that, $[^9Be]_{diss}$ remain relatively constant at a value of about 0.11 nM at mid-salinity (5–20 PSU), despite increasing dilution by seawater. In the stratified zone, $[^9Be]_{diss}$ in the surface water decrease further, except for one sample collected at station C11. In contrast, in bottom water, no obvious decrease is observed in this zone until a salinity of 34 PSU is reached. $[^9Be]_{diss}$ in bottom waters are much higher than that in surface waters at the same salinities.

3.3. Particulate ^9Be

To detect changes in the ^9Be distribution in different chemically extractable fractions of the SPM during estuarine mixing, we calculated the $[^9Be]$ in each fraction relative to the bulk particulate weight (i.e., initial mass of bulk particulates before leaching). Results are shown in Fig. 4 and Table S2. We found less than 1 ‰ of total ^9Be to be present in the "ex" fraction. Note that data for the "ex" fraction is not available for all samples due to sometimes insufficient sample size. Around 29 % to 34 % of ^9Be is bound with the "reac" fraction. The organic ^9Be only accounts for 1 % to 2 % of total particulate Be. Most ^9Be (64 % to 69 %) is retained in the "min" fraction.

Along the Changjiang-Estuary-Shelf Transect, the exchangeable $[^9Be]$ ($[^9Be]_{ex}$) is somewhat higher in fresh water-SPM (C5S and C5B) than in saline water-SPM (Fig. 4). The $[^9Be]_{reac}$ displays a slight hump at C6-1 and C6-2 stations at around 1–6 PSU. The $[^9Be]_{org}$ remains generally constant within a range of 0.02 to 0.04 μg/g, whereas in the "min" fraction, $[^9Be]_{min}$ varies from 1.22 to 1.63 μg/g with no clear trend along the transect.

3.4. Specific surface area, mineral and major elemental composition of SPM

The specific surface area of the Changjiang Estuary SPM ranges from 16.14 to 27.92 m^2/g along the salinity gradient (Table S3). Fresh water-SPM (C5S and C5B) shows lower specific surface area (17.04 m^2/g on average) than saline water-SPM (24.21 m^2/g on average). The mineral composition comprises mainly quartz, plagioclase (albite-rich), k-feldspar (microcline-rich), illite, chlorite, kaolinite and calcite (Fig. S1). No significant variation in mineral composition along the salinity gradient can be observed from the XRD pattern (Fig. S1).

Major elemental data of all chemically extractable fractions (expressed relative to the initial mass of bulk particles, in μg/g) are provided in Table S2. For all samples, the majority of the "ex" fraction is composed of Ca (15–27 % of the total Ca amount in bulk samples) and Mn (6–9 %). For SPM sampled from saline waters, the "ex" fraction also contains a non-negligible amount of Mg and Na (5–10 %). Concentrations of the other major elements are generally depleted (<2%) in this fraction. The "reac" fraction contributes up to 60–80 % of total Ca and Mn, indicating the dissolution of calcite and Mn-(oxy)hydroxides during leaching. Other elements are lower (Fe 27–33 %, Mg 42–49 %, Al 5–6 %, K and Na < 4 %) in this fraction. For the "org" fraction, all elemental concentrations analyzed are negligible (<1%) compared to the bulk concentration. The "min" fraction comprises most of bulk for Na (89–99 %), K (95–98 %), Al (94–95 %), and less for Fe (70–72 %), Mg (51–53 %), Mn (15–17 %) and Ca (6–10 %).

4. Discussion

We will now firstly discuss the changes in particulate and dissolved ^9Be concentrations along the salinity gradient, respectively, as well as the underlying control mechanisms. Building upon this, we then discuss implications for ^9Be pathways into oceans.

4.1. Particulate ^9Be distribution

The distribution of ^9Be among various chemically-extracted phases represents distinct reservoirs capable of removing or releasing ^9Be from/into seawater during estuarine mixing or after deposition onto the seafloor. In the exchangeable phase where the adsorption–desorption process predominantly controls ^9Be behavior, significant negative correlations are apparent between $[^9Be]_{ex}$ and $[K]_{ex}$, $[Mg]_{ex}$, $[Na]_{ex}$, respectively (Fig. 5), suggesting that Be^{2+} is competing with K^+, Mg^{2+}

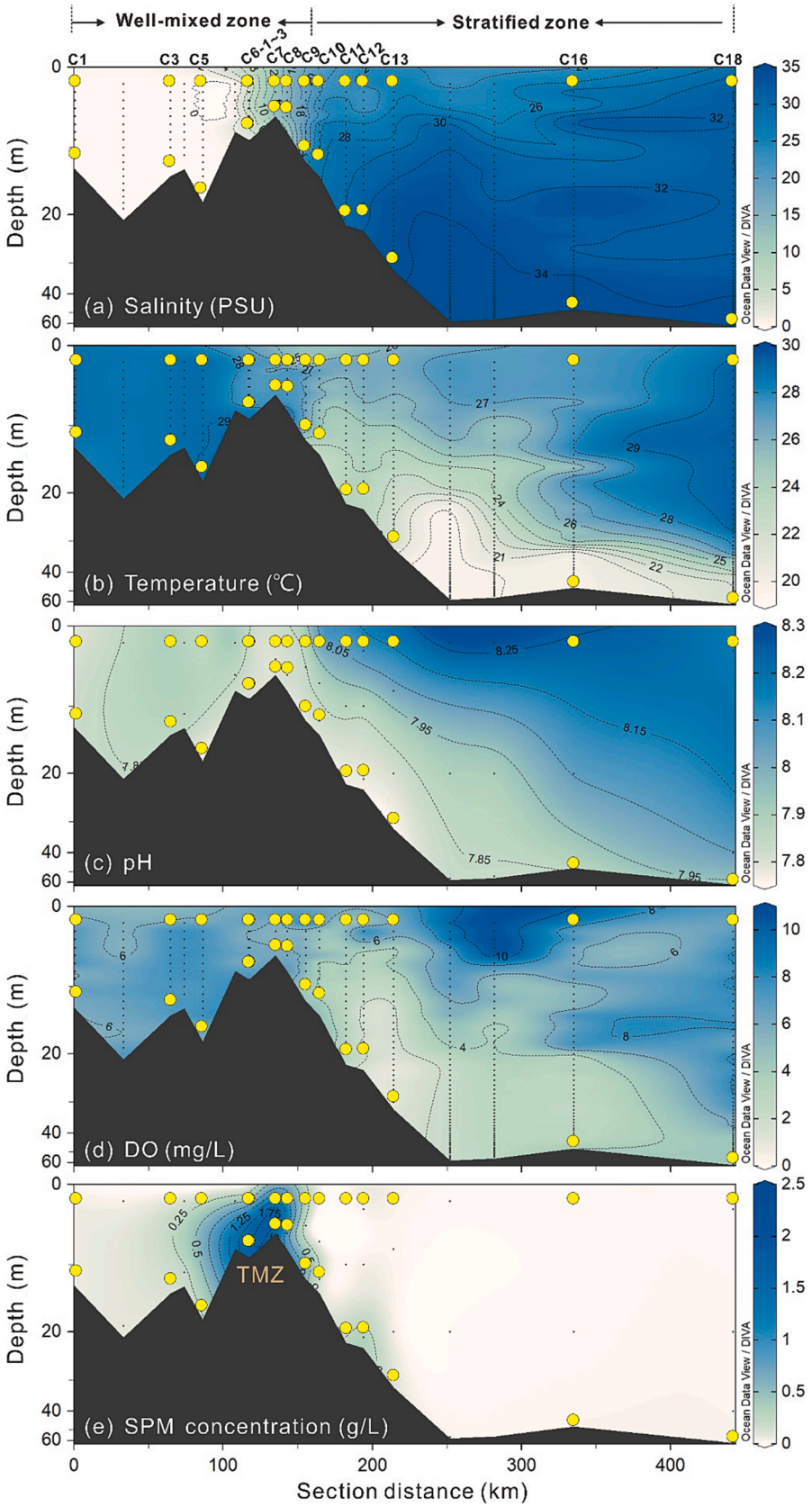

Fig. 2. Physical and chemical properties of the water column along the Changjiang-Estuary-Shelf Transect from station C1 to C18: (a) practical salinity, (b) in-situ temperature, (c) pH, (d) dissolved oxygen concentration (DO), (e) suspended sediment concentration (SPM concentration). Blank vertical dots in the figures represent sampling sites of the KECES cruise, and yellow circles represent the sampling sites for dissolved ^{9}Be measurement in this study. The depth of the ocean floor shown is not on a linear scale. TMZ: turbidity maximum zone.

Table 1
Hydrological parameters and ^{9}Be concentrations in the surface and bottom waters along the Changjiang-Estuary-Shelf Transect.

Sample ID	Longitude (°E)	Latitude (°N)	Section distance (km)	Water depth (m)	Salinity (PSU)	Temperature (℃)	pH	Suspended Particulate Matter (SPM) concentration (g/L)	DO (mg/L)	Dissolved ^{9}Be (nM)	DIP (μM)
C1S	121.06	31.78	0	1	0.0	28.9	7.80	0.045	6.35	0.144	0.55
C1B	121.06	31.78	0	11	0.0	28.9	7.83	0.058	6.45	0.152	0.75
C3S	121.57	31.40	64.5	1	0.0	28.8	7.90	0.097	5.97	0.122	0.49
C3B	121.57	31.40	64.5	12	0.0	28.9	7.87	0.199	6.96	0.131	0.57
C5S	121.75	31.29	85.9	1	0.0	28.9	7.84	0.199	6.04	0.136	0.45
C5B	121.75	31.29	85.9	16	0.0	29.1	7.78	0.280	7.47	0.143	0.79
C6-1S	121.97	31.09	116.5	1	1.0	28.1	7.84	n.d.	6.21	0.126	1.18
C6-2S	121.98	31.09	117.2	1	4.1	27.8	7.83	0.384	5.86	0.098	1.62
C6-2B	121.98	31.09	117.2	7	6.2	27.4	7.79	2.078	6.68	0.113	1.81
C6-3S	121.99	31.08	118.0	1	9.4	26.9	7.83	0.479	6.62	0.107	1.55
C6-3B	121.99	31.08	118.0	7	9.1	26.9	7.84	1.541	6.28	0.112	1.49
C7S	122.15	31.03	135.2	1	12.5	27.3	7.81	1.141	5.80	0.118	1.11
C8S	122.24	31.02	142.9	1	14.4	27.5	7.84	n.d.	5.52	0.110	0.81
C8B	122.24	31.02	142.9	6	14.9	27.5	7.83	n.d.	5.95	0.118	1.23
C9S	122.36	31.00	155.5	1	16.9	22.2	7.84	n.d.	5.94	0.097	1.10
C9B	122.36	31.00	155.5	10	17.8	26.8	7.80	0.838	5.05	0.108	0.95
Boundary between well-mixed zone and stratified zone											
C10S	122.45	30.97	164.6	1	21.9	26.9	8.08	0.016	6.39	0.048	0.23
C10B	122.45	30.97	164.6	12	26.7	25.1	7.82	0.035	3.74	0.098	0.69
C11S	122.62	30.92	188.9	1	24.2	24.3	8.06	0.017	4.62	0.087	0.21
C11B	122.62	30.92	188.9	20	30.0	23.6	7.78	0.200	3.65	0.096	0.73
C12S	122.74	30.94	200.9	1	22.3	26.6	8.11	0.048	8.11	0.032	0.15
C12B	122.74	30.94	200.9	21	31.0	24.0	7.78	0.366	2.08	0.094	0.79
C13S	122.89	30.81	221.4	1	26.0	26.4	8.16	0.024	6.04	0.039	0.22
C13B	122.89	30.81	221.4	30	33.6	22.1	7.76	0.016	1.62	0.082	0.80
C16S	124.00	30.30	342.1	1	25.5	27.4	8.24	0.008	8.32	0.021	0.08
C16B	124.00	30.30	342.1	46	34.6	20.1	7.87	0.024	3.38	0.046	0.71
C18S	124.99	29.87	449.2	1	32.0	29.4	8.17	0.005	6.63	0.030	0.03
C18B	124.99	29.87	449.2	62	34.4	24.0	7.93	0.026	4.61	0.039	0.58

The suffix "S" and "B" in sample ID indicate "surface water" and "bottom water", respectively.
n.d. = not determined.
PSU = practical salinity units, in permill; DO = dissolved oxygen; DIP = dissolved inorganic phosphorus (DIP taken from Xu et al. (2021)).

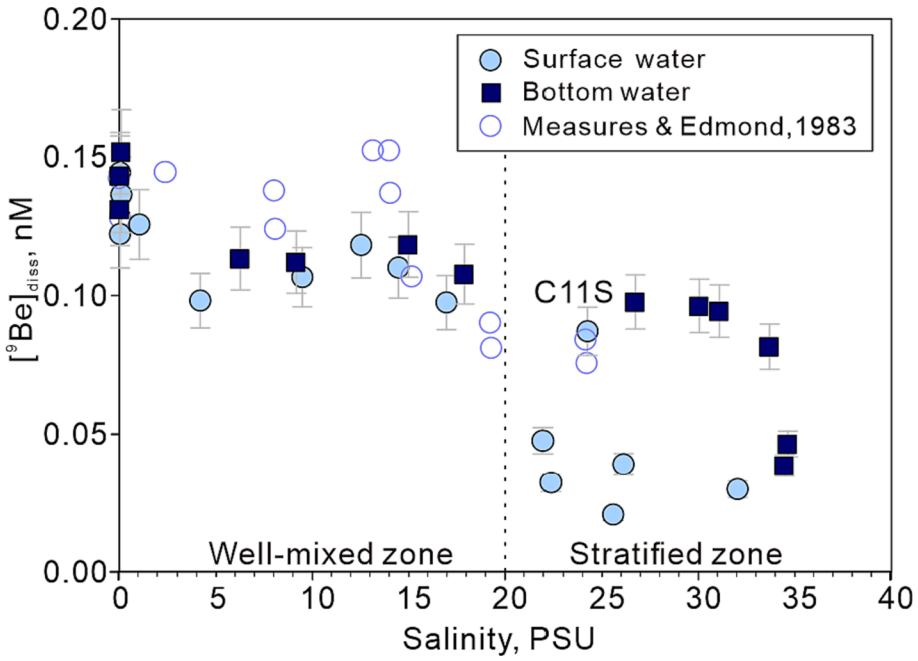

Fig. 3. Dissolved ^{9}Be concentrations along the salinity gradient of the Changjiang-Estuary-Shelf Transect of this study compared to surface data from Measures and Edmond (1983) (for that study, no uncertainty estimates are available). A 10% uncertainty is given that represents the long-term recovery for iron co-precipitation method.

and Na^{+} via ion exchange during estuarine mixing. Within the "reac" fraction, $[^{9}Be]_{reac}$ shows a significant positive correlation with $[Al]_{reac}$, $[Mg]_{reac}$ and $[Fe]_{reac}$, but a negative correlation with $[Ca]_{reac}$ (Fig. 5), indicating the variation of $[^{9}Be]_{reac}$ is closely associated with the enrichment of Al, Mg and Fe-(oxy)hydroxides and dilution by carbonate. This implies that Al, Mg and Fe-(oxy)hydroxides serve as primary carrier

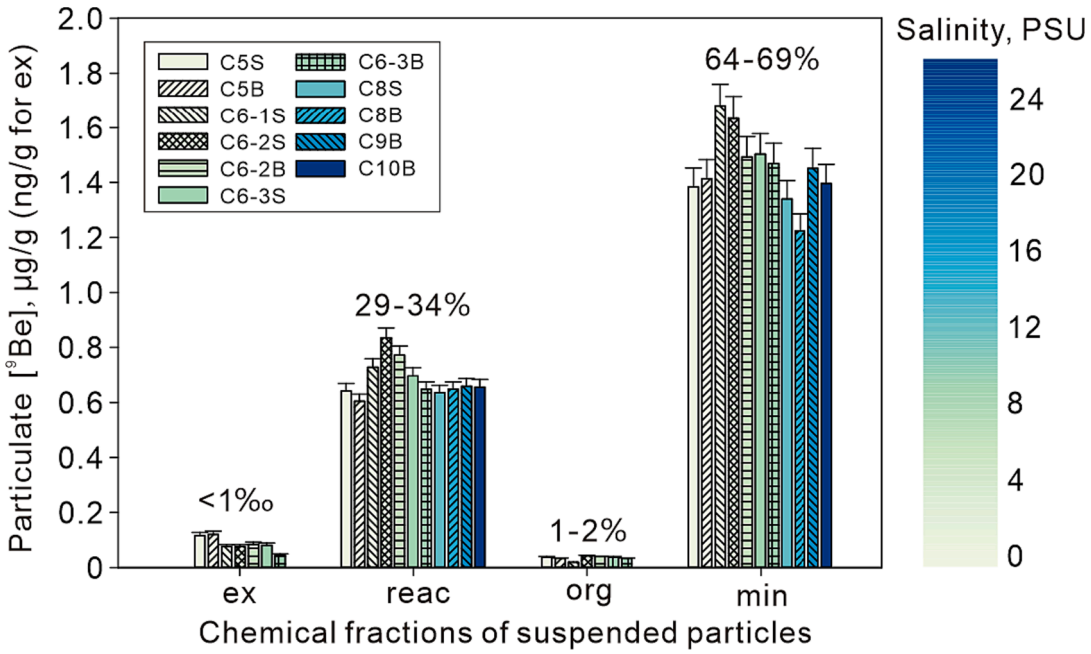

Fig. 4. Particulate ^{9}Be concentrations in different chemical fractions along the Changjiang-Estuary-Shelf Transect. The percentages give the proportion of ^{9}Be in each fraction relative to the total (sum of all fractions).

of ^{9}Be, and thus the mobility of reactive ^{9}Be is probably influenced by redox conditions. While the $[^9Be]_{org}$ remains almost constant along the transect (see section 3.3), the $[^9Be]_{min}$ shows a significant positive linear correlation with $[Al]_{min}$, $[K]_{min}$, $[Mg]_{min}$ and $[Fe]_{min}$ (Fig. 5). Based on the mineral composition of SPM in the Changjiang Estuary (Fig. S1), we infer that the variation in [^{9}Be] in the silicate residue is likely a consequence of the relative predominance of plagioclase feldspars, as carrier of primary ^{9}Be (Ryan, 2002).

Based on the distribution of ^{9}Be between chemically-extracted and dissolved phases, we infer that the variations of [^{9}Be] in the "reac" and "min" fractions are the result of physical mineral sorting rather than chemical water-particle interactions, given that the dissolved ^{9}Be pool is two orders of magnitude smaller than the "reac" and "min" pools (Fig. 6). The fact that [^{9}Be] in the "reac" and "min" fractions do not change drastically with distance from land (Table 1) demonstrates that mineral sorting in estuaries is not solely controlled by transportation distance, but also by other factors, such as sediment re-suspension due to e.g., tidal influence.

While water-particle interactions during estuarine mixing unlikely affect the "reac" and "min" pools, in turn, they may significantly impact the dissolved and exchangeable ^{9}Be pools (Fig. 6). Therefore we will mainly focus on the changes in dissolved and exchangeable [^{9}Be] and the underlying controlling mechanisms in the forthcoming discussion.

4.2. Quantification of dissolved ^{9}Be behavior with a three end-member mixing model

Dissolved ^{9}Be along the Changjiang-Estuary-Shelf Transect shows a non-conservative behavior with complex removal and release patterns, depending on salinity and oceanographic setting (i.e., well-mixed vs. stratified zone, Fig. 3). To quantify the removal and release of dissolved ^{9}Be during estuarine mixing, we first calculate the theoretical conservative concentrations of dissolved ^{9}Be at each station that would result if changes in $[^9Be]_{diss}$ solely were a consequence of physical water-mass mixing. In a diagram of potential temperature versus salinity (Fig. 7), all the data from the Changjiang-Estuary-Shelf Transect fall into the interior of a triangular space (outlined in grey, Fig. 7), suggesting the mixing of three end-members (Renner, 1989; Tomczak, 1981). We define the three end-members as Changjiang Diluted Water (CDW), Taiwan Warm Current Surface Water (TWCSW), and Taiwan Warm Current Deep Water (TWCDW) according to their specific potential temperatures and salinities. This classification of end-members is consistent with previous studies (Wang et al., 2021; Zhang et al., 2014). The surface water collected at station C11 shows a similar origin as the bottom water (Fig. 7), indicating the development of upwelling in this area.

We thus calculate the theoretical conservative concentrations of dissolved ^{9}Be using a three-endmember mixing model (see supplementary material). The extent of ^{9}Be removal/release compared to conservative mixing is described by $\Delta[^9Be]_{diss}$, i.e., the difference between observed values ($[^9Be]_{measured}$) and values predicted by the mixing model. We interpret negative values of $\Delta[^9Be]_{diss}$ such that removal processes dominate over release processes, while positive values suggest the opposite.

Results of this mixing model (Fig. 8, Table S4) suggest that in the well-mixed zone, the dissolved ^{9}Be is first dominated by removal processes when salinity increases from 0 to 5 PSU (designated as low-salinity range thereafter to enhance clarity for subsequent discussions), but is gradually dominated by release processes from 5 to 20 PSU (designated as mid-salinity range thereafter). In the stratified zone ($S > 20$ PSU), we note that $\Delta[^9Be]_{diss}$ shows removal from surface waters, except one outlier for surface water C11S evidently affected by coastal upwelling, while ^{9}Be release is evident in bottom waters.

4.3. Mechanisms controlling the removal or release of dissolved ^{9}Be

A number of potential mechanisms may contribute to the removal or release of dissolved ^{9}Be during estuary mixing. These include 1) adsorption and desorption onto/from particle surfaces (see section 4.3.1), 2) flocculation/deflocculation of colloids (section 4.3.2), and 3) porewater diffusion/expulsion and submarine groundwater discharge, which are part of the "benthic flux" pathway (section 4.3.3), and are hence conceptually lumped together in this study. Next we will identify the potential controlling processes based on the relationships between $\Delta[^9Be]_{diss}$ and the particulate [^{9}Be] in relation to the corresponding water physicochemical parameters.

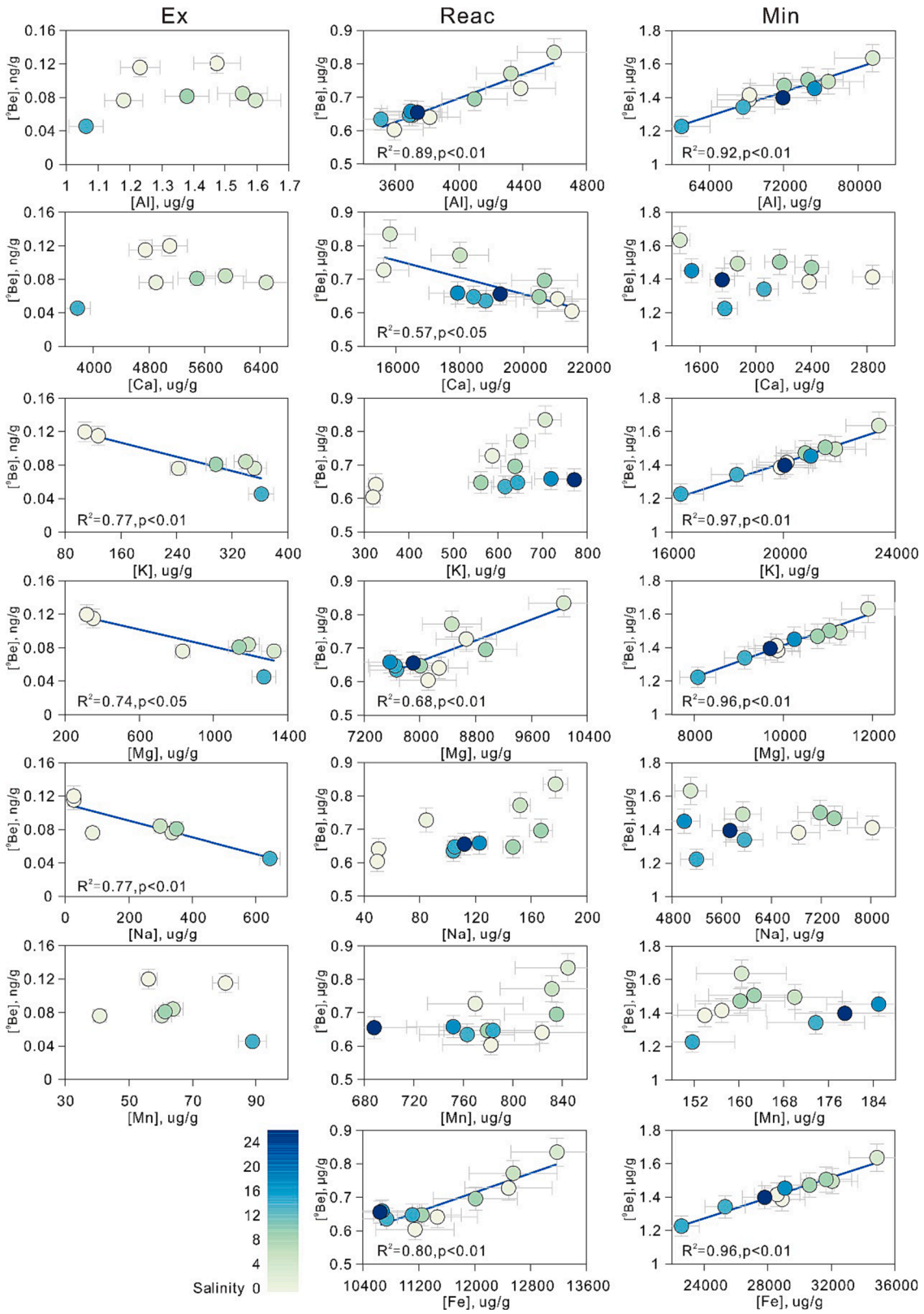

Fig. 5. ^{9}Be concentrations (color-coded for salinity) vs. major elemental concentrations in exchangeable (ex), reactive (reac) and silicate residue (min) fractions of SPM. The linear regression line is only shown when R^2 (the coefficient of determination, i.e., the squared correlation coefficient) > 0.5. Fe concentrations were below the detection limit for the "ex" fraction.

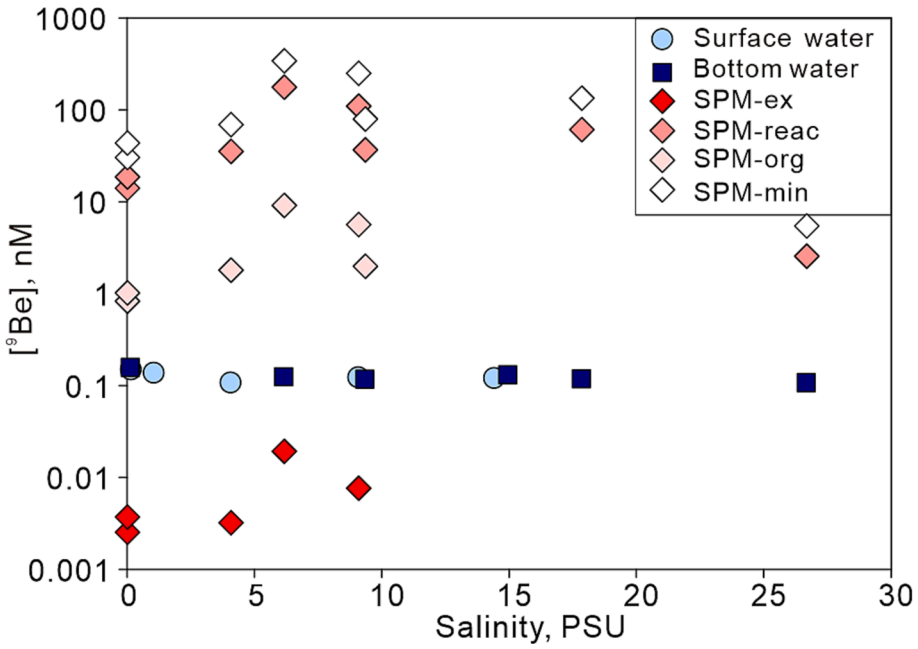

Fig. 6. ^{9}Be distribution in the different chemically-extracted phases of SPM (calculated by forming the product of [^{9}Be] in each fraction (μg/g) times the SPM concentration (in g/L, Table 1) and in the dissolved phase. Error bars are smaller than symbol size.

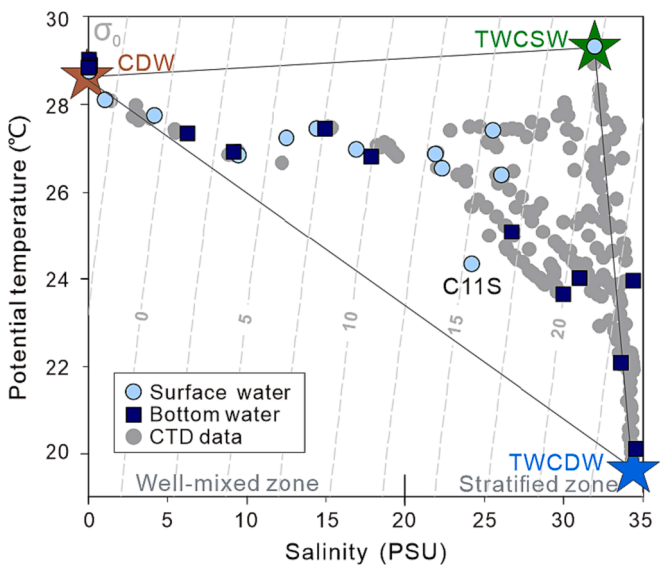

Fig. 7. Salinity vs. potential temperature (S-T) plot with potential density isopycnals (σ_0, dotted gray lines) along the Changjiang-Estuary-Shelf Transect. The gray dots are CTD profile data from all stations, whereas the light blue circles and dark blue squares represent samples measured for ^{9}Be in this study. The brown, green and blue stars indicate three water endmembers: Changjiang Diluted Water (CDW), Taiwan Warm Current Surface Water (TWCSW), and Taiwan Warm Current Deep Water (TWCDW), respectively.

4.3.1. *Adsorption-desorption*

Many studies have demonstrated the significance of sorption onto SPM in controlling the dissolved concentrations of trace metals in estuaries. As ionic strength increases at low to mid-salinity, desorption of metals from SPM is induced. Such desorption is thought to present an important source for trace elements such as Ba and Ra (Cao et al., 2021; Li et al., 2021; Li et al., 1984b; Samanta and Dalai, 2016; Tipper et al., 2021). Given that most Be adsorption–desorption occurs within one day (Boschi and Willenbring, 2016; Li et al., 1984a; You et al., 1989), and if adsorption–desorption is the dominating process functioning at low to mid-salinity, we expect the $\Delta[^{9}Be]_{diss}$ and the corresponding particulate $[^{9}Be]_{ex}$ to inversely correlate. However, previous studies have shown that sorbed Be concentrations tend to increase with increasing specific surface area (SSA) (Aldahan et al., 1999, Willenbring and von Blanckenburg, 2010, Shen et al., 2004), or even correlate with SSA (Boschi and Willenbring, 2021). Considering this, we normalize $[^{9}Be]_{ex}$ for specific surface area (termed $[^{9}Be]_{ex\_normalized}$, in pmol/m^2) as a first-order method to eliminate the effect of changing surface area, potentially induced by estuarine mineral grain sorting, on sorbed Be concentrations. The $[^{9}Be]_{ex\_normalized}$ and $\Delta[^{9}Be]_{diss}$ both show a steep decline at low salinity followed by an increase at 4–10 PSU for all samples, except the $[^{9}Be]_{ex\_normalized}$ datapoint at ca. 12 PSU (Fig. 8). The drop of $[^{9}Be]_{ex\_normalized}$ at the onset of mixing indicates ^{9}Be desorption from SPM into the dissolved phase, which is likely caused by desorption of ^{9}Be via ion exchange with K^+, Mg^{2+} and Na^+ stemming from seawater as mentioned in section 4.1. Hence, the removal of dissolved ^{9}Be at low salinity cannot be explained with ^{9}Be adsorption onto SPM, implying 1) another mechanism is operating and 2) that the exchangeable pool of river-borne ^{9}Be available for desorption is too small (ca. 0.003 nM, Fig. 6) to counterbalance the initial removal of dissolved ^{9}Be. Although at mid-salinity the ^{9}Be exchangeable pool becomes larger due to higher SPM concentrations (Fig. 6), overall increasing $[^{9}Be]_{ex\_normalized}$ at 4–10 PSU (Fig. 8) suggest that ^{9}Be is not desorbed from, but instead, rather adsorbed onto SPM. As such, neither the ^{9}Be removal nor release observed in the well-mixed zone is likely a consequence of direct ^{9}Be adsorption–desorption, implying that other processes are at play.

The above analysis cannot be done in the stratified zone as we lack $[^{9}Be]_{ex}$ data. Previous studies have shown that in addition to the ionic strength of the liquid, the sorption behavior of Be is also dependent on pH and the composition of solid and liquid (Aldahan et al., 1999; Boschi and Willenbring, 2016; You et al., 1989). Although pH ranges from 7.76 to 8.24 in our study area, numerous studies on the sorption behavior of Be under different pH conditions have shown that no further adsorption–desorption occurs at pH values of approximately 7 to 9 (de Bruin et al., 1963; You et al., 1989; Veselý et al., 2002; Zhao et al., 2022). This suggests that the pH-associated adsorption–desorption process is unlikely the dominate process regulating the dissolved ^{9}Be behavior in the higher-salinity stratified zone.

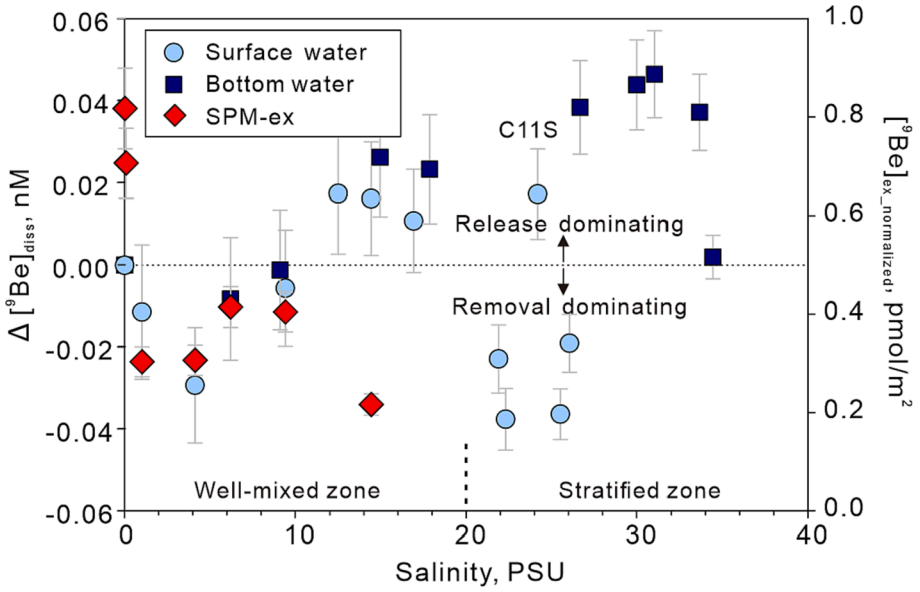

Fig. 8. The difference of measured dissolved ^{9}Be concentration relative to conservative mixing ($\Delta[^{9}Be]_{diss}$, calculated from supplemental eqs. 1–5), compared to the exchangeable ^{9}Be concentration in the corresponding SPM (normalized by surface area, in pmol/m^2) along the Changjiang-Estuary-Shelf Transect. The uncertainty of $\Delta[^{9}Be]_{diss}$ is propagated from the analytical uncertainty of each sample and the three endmembers (see supplementary material). An analytical uncertainty of 10% for $[^{9}Be]_{ex}$ and of 1.1% for specific surface area is propagated to the uncertainty of $[^{9}Be]_{ex\_normalized}$.

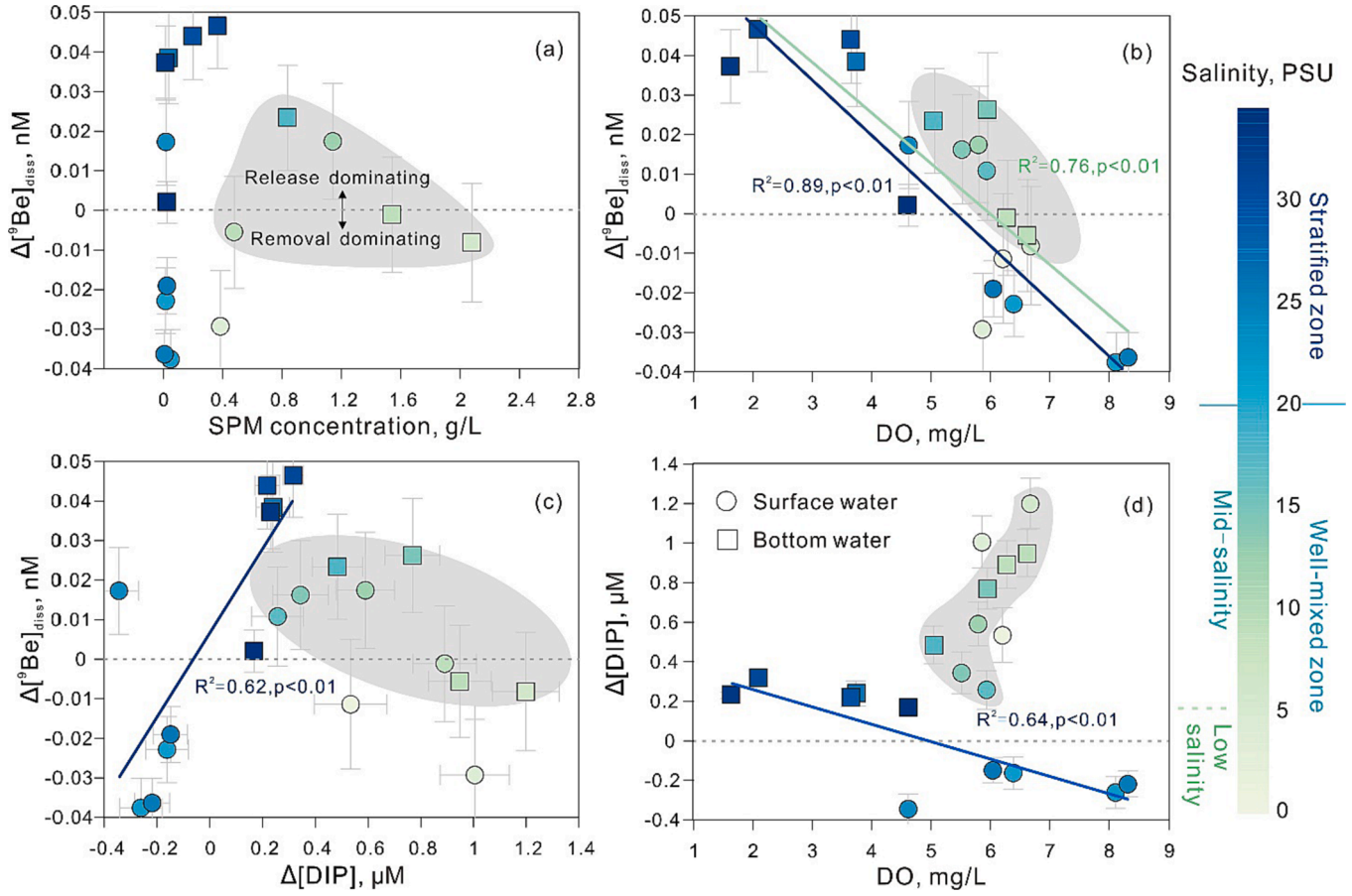

Fig. 9. $\Delta[^{9}Be]_{diss}$ color-coded for salinity vs. (a) SPM concentration, (b) DO (dissolved oxygen), (c) Δ[DIP] (bio-chemically altered fraction of dissolved inorganic phosphorus), and (d) Δ[DIP] vs. DO. SPM concentration data are not available for some stations. The DIP data are from Xu et al. (2021). The Δ[DIP] are calculated according to supplemental eqs. 1–5 with [DIP] substituted for $[^{9}Be]_{diss}$. The grey shaded area indicates data from the mid-salinity range, the green line represents the regression results for all data points (excluding those from the low salinity zone, as there, $[^{9}Be]_{diss}$ are considered to be influenced by colloidal flocculation), and the dark blue line represents regressions only for data from the stratified zone (S > 20 PSU).

4.3.2. Colloidal flocculation-deflocculation

Colloidal flocculation has been invoked to cause removal of particle-reactive elements at low salinity. When river water starts mixing with seawater, the seawater cations will reduce the negative surface-charge of riverine nanoparticles and colloids, inducing flocculation (Boyle et al., 1977). This phenomenon has been widely investigated in the laboratory and field (e.g., Andersson et al., 2001; Coffey et al., 1997; Merschel et al., 2017; Rousseau et al., 2015; Sholkovitz and Szymczak, 2000). Since adsorption of ^{9}Be onto SPM evidently does not control the removal of dissolved ^{9}Be in the Changjiang Estuary (section 4.3.1), we suggest that the salt-induced colloidal flocculation is likely the predominant driver of low-salinity removal of dissolved ^{9}Be, as shown for other particle-reactive elements such as Fe and REEs in the Changjiang Estuary (Wang and Liu, 2003, 2008).

In contrast, the colloidal deflocculation seems unlikely to account for the release of ^{9}Be at mid-salinity. Wang and Liu (2003) suggested that the release of Fe and REEs at mid-salinity in the Changjiang Estuary might result from intense sediment re-suspension, potentially leading to desorption and/or disruption of the coagulation process. However, we observe no correlation between $\Delta[^{9}Be]_{diss}$ and SPM concentration, i.e., neither across the entire salinity range, nor within specific ranges, such as the mid-salinity range (Fig. 9a). Note that this absent correlation between $\Delta[^{9}Be]_{diss}$ and SPM concentration also implies that the Be scavenging rate is not a function of increased SPM concentrations as suggested by Li et al. (2021).

In summary, our results suggest that the removal of dissolved ^{9}Be at low salinity is likely caused by salt-induced colloidal flocculation, consistent with other particle-reactive elements. The release of dissolved ^{9}Be at mid-salinity however cannot be associated with colloidal deflocculation or ^{9}Be desorption (see section 4.3.1). We thus next inspect the role of benthic processes in controlling the release of ^{9}Be in this salinity range.

4.3.3. Redox-related benthic Be flux at mid and high salinities

We observe a significant inverse correlation between $\Delta[^{9}Be]_{diss}$ and dissolved oxygen (DO) at mid-high salinities (indicated by the green line in Fig. 9b), as well as in the high salinity region (i.e., the stratified zone, indicated by the dark blue line). Moreover, we also note a positive correlation between $\Delta[^{9}Be]_{diss}$ and Δ[DIP] (bio-chemically altered fraction of dissolved inorganic phosphorus) (Fig. 9c), together with an inverse correlation between Δ[DIP] and DO (Fig. 9d) in the stratified (blue line) zone. Similar to $\Delta[^{9}Be]_{diss}$, negative values of Δ[DIP] indicate the removal of DIP, potentially attributed to biological utilization, whereas positive values indicate release, possibly originating from organic matter decomposition or reduction of iron (oxy)hydroxides. Hence, the pronounced correlations between $\Delta[^{9}Be]_{diss}$ and Δ[DIP], as well as Δ[DIP] and DO (Fig. 9c, d) suggest that in the stratified zone: 1) higher DO levels in the surface waters are associated with the removal of both ^{9}Be and DIP, while 2) lower DO levels in bottom waters appear to facilitate the release of ^{9}Be and DIP to the dissolved phase. From this pattern, we invoke that the dissolved ^{9}Be behavior in the stratified zone is regulated by similar mechanisms as DIP. The related mechanisms we discuss now for 1) surface waters and 2) bottom waters in the stratified zone, respectively.

1) The removal of DIP from oxygen-rich surface waters of the stratified zone is considered to be the result of extensive DIP consumption due to phytoplankton blooms (Liu et al., 2022). This is further evidenced by higher chlorophyll-a concentrations observed in the same set of samples in this region (Xu et al., 2021). Although Be is not an essential nutrient for phytoplankton growth (Sunda, 2012), high biological productivity may facilitate the scavenging of Be (Kusakabe et al., 1990; Xu, 1994), resulting in the observed negative values for $\Delta[^{9}Be]_{diss}$.
2) The release of ^{9}Be and DIP into low-oxygen bottom waters is likely regulated by reduction of Fe-Mn(oxy)hydroxides during early diagenesis, as evidenced by porewater profiles of ^{9}Be (Deng et al., 2023) and DIP (Liu et al., 2020) in the Changjiang Estuary. It has been observed that elevated benthic P flux in the Changjiang Estuary is associated with hypoxic conditions (Liu et al., 2020). A similar relationship may also exist for Be, given the significant inverse correlation between $\Delta[^{9}Be]_{diss}$ and DO (Fig. 9b). Intensified hypoxic conditions, as evident by decreased DO in bottom water, may favor the diagenetic release of ^{9}Be in two ways:
   i) Hypoxic conditions tend to shift the oxygen penetration depth upwards in the sediment column, potentially allowing the elevated $[^{9}Be]_{diss}$ in reduced porewaters to be present close to the sediment–water interface (Fig. 10 columns A and B). This would lead to a more efficient upward migration of dissolved ^{9}Be released from sediments to overlying water, as observed for other trace metals (Liu et al., 2022; Shi et al., 2019). Such behavior is further supported by observations from dissolved [Fe], [Mn] and [Nd] in porewater profiles along the Changjiang-Estuary-Shelf Transect (Deng et al., 2022), where maximum concentrations were observed at shallower depths (~5 cm) for station C13 (in the center of the hypoxia zone), whereas for the well-oxygenated C6-1 station, concentration maxima occurred at a much deeper depths of >20 cm (Deng et al., 2022).
   ii) Low oxygen levels, together with low pH and low temperatures in the bottom seawater (Fig. 2), may markedly slow down the oxidation rate of released Fe(II) and Mn(II) in porewater during early diagenesis (Lohan and Bruland, 2008; Millero et al., 1987; Sunda and Huntsman, 1987). A consequence would be that less Fe-Mn (oxy)hydroxides are formed that are able to scavenge released dissolved ^{9}Be during its upward migration from porewater into the water column (Fig. 10 columns A and B).

We suggest that the release of ^{9}Be at mid-salinity is dominated by the same benthic processes as observed in bottom waters of the stratified zone, since other processes including colloidal deflocculation or ^{9}Be desorption have been ruled out (section 4.3.2). Unlike in the stratified zone where benthic sources only contribute to bottom waters due to the strong water stratification, the release of ^{9}Be at mid-salinity is impacting $[^{9}Be]_{diss}$ in both surface and bottom waters. This is likely a consequence of strong vertical water mixing at mid-salinity, as in this region the turbidity maximum zone developed (Fig. 10). The effect is similar to what we observed at station C11 where upwelling led to $[^{9}Be]_{diss}$ in surface water that is identical to bottom water.

In addition to the diagenetic release of ^{9}Be, another potential benthic contributor could be the submarine groundwater discharge (including fresh groundwater, re-circulating seawater and a composite of the two), which is considered an important source of nutrients (e.g., DIP) to the coastal ocean (e.g., Wang et al., 2018). On the other hand, submarine groundwater discharge may also contribute to the formation of hypoxic zones (e.g., Guo et al., 2020), as it is characterized by lower DO levels resulting from substantial organic matter decomposition and oxygen isolation (Gagan et al., 2002). As a result, the elevated $\Delta[^{9}Be]_{diss}$ under low DO conditions along the Changjiang-Estuary-Shelf Transect could potentially be attributed to an increase in submarine groundwater discharge. Although $[^{9}Be]_{diss}$ data are not available for the groundwater end-member in the study area, reported $[^{9}Be]_{diss}$ in groundwater tend to be higher than in river water (Dannhaus et al., 2018; Shravanraj et al., 2021; Vesely et al., 2002). Thus, it is possible that submarine groundwater discharge also plays a role in contributing excess dissolved ^{9}Be into the water column. However, given the minor temperature and salinity differences between submarine groundwater and the coastal seawater at the permeable Changjiang coast (Jiang et al., 2021), this potential endmember can hardly be distinguished by the S-T plot (Fig. 7).

To summarize, in light of the strong correlations between $\Delta[^{9}Be]_{diss}$ and DO, as well as Δ[DIP] in the stratified zone, we propose that the benthic flux is the main contributor to the release of ^{9}Be at mid-salinity

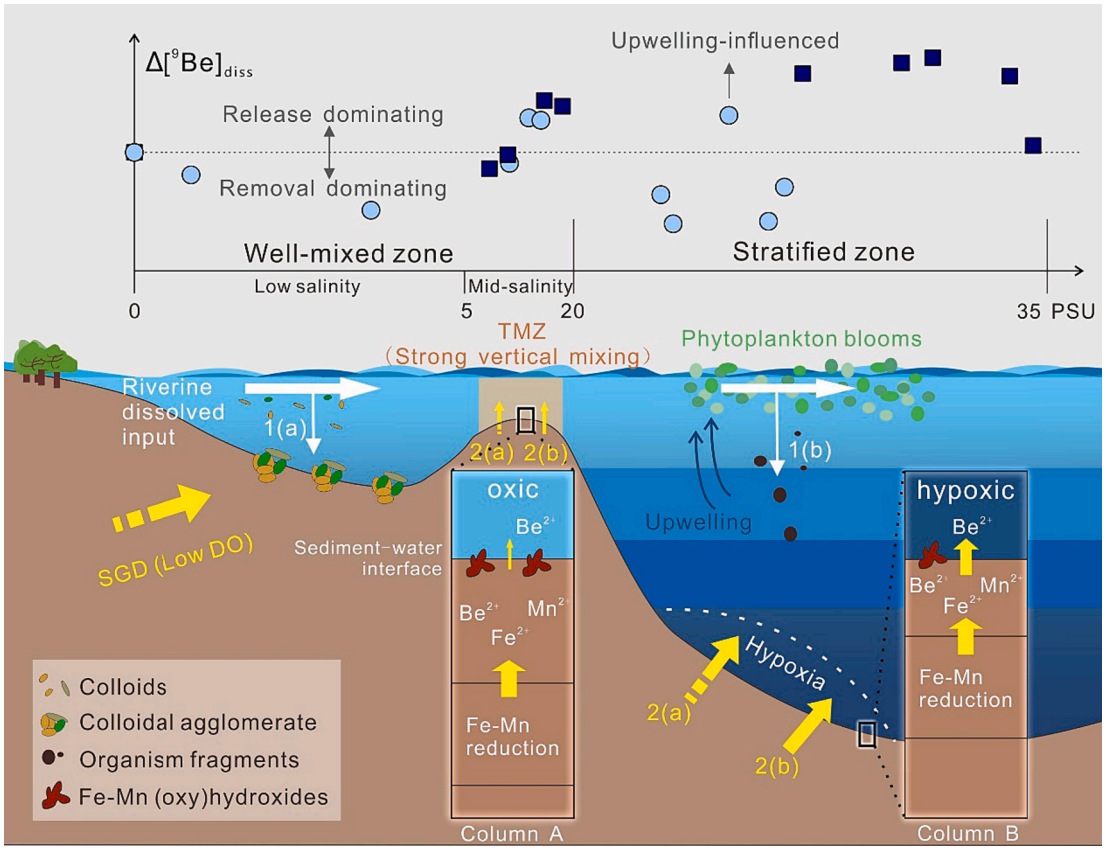

Fig. 10. Schematic illustration of different pathways of dissolved ^{9}Be through the Changjiang Estuary into the ocean. TMZ: turbidity maximum zone; SGD: submarine groundwater discharge; DO: dissolved oxygen. The white arrow represents the riverine dissolved ^{9}Be input and two associated removal processes are indicated as: 1 (a) colloidal flocculation, 1(b) biological scavenging. Yellow arrows represent potential benthic pathways supplying ^{9}Be into seawater: 2(a) SGD (dashed arrow) and 2(b) porewater diffusion/expulsion (solid arrow). The thickness of the yellow arrow scales with the magnitude of the flux. Column A- oxic conditions in TMZ; column B- hypoxic conditions at high salinities.

and into bottom waters of the stratified zone. Possible processes include porewater diffusion/expulsion and submarine groundwater discharge. The enhanced benthic flux of ^{9}Be seems to occur in the hypoxic zone. In contrast, the removal of ^{9}Be from surface waters of the stratified zone is likely a result of biological scavenging facilitated by phytoplankton blooms.

4.4. *Implications for ^{9}Be pathways into oceans*

The complex behavior of dissolved ^{9}Be along the Changjiang-Estuary-Shelf Transect implies the co-existence of different pathways of terrigenous ^{9}Be input into the ocean. In addition to the two major pathways proposed by von Blanckenburg and Bouchez (2014) and von Blanckenburg et al., (2015,2022), i.e., dissolved riverine ^{9}Be fluxes escape coastal scavenging (path 1) and reactive riverine particulate-bound ^{9}Be is released from bottom sediment into seawater (path 2), our exchangeable ^{9}Be data suggest a rapid desorption of ^{9}Be from SPM through cation exchange at the onset of estuarine mixing (Fig. 8). However, the ^{9}Be input through this path is negligible relative to the overall ocean Be budget, as the exchangeable ^{9}Be carried by riverine SPM is two orders of magnitude lower than that in the dissolved phase (Fig. 6, S = 0). With respect to path 1, we suggest that colloidal flocculation occurring at low-salinity and biological scavenging resulting from seasonal phytoplankton blooms may modify the ^{9}Be input through this pathway, whereas increases in SPM concentrations do not necessarily promote ^{9}Be scavenging in contrast to the hypothesis of Li et al., (2021). With respect to path 2, our data offer additional support for the benthic contribution of ^{9}Be into coastal seawater. This benthic ^{9}Be flux is likely associated with the reduction of Fe-Mn (oxy)hydroxides during early diagenesis, in alignment with findings derived from pore water ^{9}Be profiles (Deng et al., 2023), but could potentially involve a contribution from submarine groundwater discharge. Moreover, the hypoxia-anoxia conditions in bottom waters may enhance the diagenetic release of ^{9}Be.

Quantifying the relative contributions of the above-mentioned two major pathways to the oceanic ^{9}Be budget is key to establishing ^{10}Be/^{9}Be as a quantitative paleo-weathering proxy. Our data shows that the reactive particulate ^{9}Be pool (i.e., $^{9}Be_{reac}$) transported into coastal ocean is more than 100 times higher than the riverine dissolved pool (Fig. 6, S = 0). This means that even if only 1 % of ^{9}Be is released from the sediment during early diagenesis, this flux will be comparable to or even exceed the dissolved flux (prior to the coastal trap). Using compiled riverine dissolved ^{9}Be fluxes (Deng et al., 2023) and the average estuarine removal rate (56 %) (Suhrhoff et al., 2019), Deng et al., (2023) calculated that about $1.8 \pm 0.4 \times 10^{7}$ mol/year of ^{9}Be is delivered to the ocean via path 1,accounting for less than 30 % of the total oceanic Be input. In this calculation, the average estuarine removal (56 %) is estimated from previously published ^{9}Be data in surface waters of six estuaries and their removal/release behavior compared to conservative mixing (Suhrhoff et al., 2019). However, our data shows that the surface water-derived ^{9}Be signal could be altered by benthic contribution in a vertically well-mixed estuary, such as the mid-salinity range in the Changjiang Estuary. This would lead to an underestimation of the estuarine removal extent, suggesting that the actual input of riverine dissolved ^{9}Be into the ocean (path 1) may be even lower than currently estimated. In turn, this suggests that benthic fluxes (path 2) could play an even more important role. If paleo-marine ^{10}Be/^{9}Be records are primarily controlled by changes in benthic ^{9}Be fluxes, ultimately changes in sediment and organic carbon delivery, as well as sea-level fluctuations

that regulate the extent of diagenesis might be first-order controlling mechanisms (Deng et al., 2023). Given that the reduction of Fe-Mn-oxyhydroxides during diagenesis is likely linked to oxygen levels in the benthic realm, changes in paleoredox could also be a key factor. On the other hand, a contribution of submarine groundwater discharge as part of the benthic flux cannot be ruled out in regulating dissolved ^{9}Be concentrations. Submarine groundwater discharge may constitute another significant, yet unexplored, source to the marine ^{9}Be budget. Therefore, identifying the various factors that govern benthic ^{9}Be flux and assessing their relative significance will be critical for firmly deciphering paleo-oceanic ^{10}Be/^{9}Be records.

5. Summary and outlook

We identify three different pathways and the underlying mechanisms for the transport of terrigenous ^{9}Be into the ocean through the Changjiang Estuary, based on systematic data for particulate and dissolved ^{9}Be along the entire salinity transect. These pathways include: 1) riverine dissolved input, 2) ^{9}Be desorption from the suspended particulate matter (SPM), and 3) coastal benthic inputs which involve porewater diffusion/expulsion and/or submarine groundwater discharge. Regarding these pathways, we show that.

1) The riverine dissolved ^{9}Be flux is reduced during estuarine mixing due to colloidal flocculation and biological scavenging resulting from seasonal phytoplankton blooms. To derive the actual riverine dissolved ^{9}Be flux to the ocean that survives the coastal trap, surface dissolved ^{9}Be data along the salinity gradient is unlikely to provide a complete quantification, because the ^{9}Be in surface waters can be altered by benthic contributions in vertically well-mixed zones.
2) The ^{9}Be flux derived from desorption from SPM through rapid cation exchange is negligible, as the exchangeable ^{9}Be pool on riverine SPM is two orders of magnitude lower than the dissolved ^{9}Be pool.
3) Benthic ^{9}Be fluxes play a crucial role in controlling the paleo-marine ^{10}Be/^{9}Be record. For a robust interpretation of the paleo-marine ^{10}Be/^{9}Be record, a more comprehensive investigation of the magnitude of benthic ^{9}Be fluxes in diverse environments is required to identify their primary controlling factors (e.g., dissolved oxygen concentration in bottom seawater or sediment/organic matter delivery). This will shed light on our understanding of how benthic Be fluxes have changed in the past and thereby how the paleo-marine ^{10}Be/^{9}Be record has responded to past environmental changes. For instance, if dissolved oxygen concentration is evidenced as a key influencing factor, the paleo-marine ^{10}Be/^{9}Be record may reflect changes in the paleo-redox conditions; however, if sediment delivery plays a more important role, this record may serve as a tracer for past continental denudation rate.

CRediT authorship contribution statement

Chenyu Wang: Conceptualization, Data curation, Formal analysis, Investigation, Methodology, Writing – original draft. **Friedhelm von Blanckenburg:** Conceptualization, Funding acquisition, Supervision, Validation, Writing – review & editing. **Ergang Lian:** Resources, Software, Writing – review & editing. **Shouye Yang:** Resources, Validation, Writing – review & editing. **Jeffrey Paulo H. Perez:** Methodology, Validation, Writing – review & editing. **Hella Wittmann:** Conceptualization, Funding acquisition, Supervision, Validation, Writing – review & editing.

Declaration of competing interest

The authors declare that they have no known competing financial interests or personal relationships that could have appeared to influence the work reported in this paper.

Acknowledgements

We thank Chengfan Yang, Zheng Lai, Zhan Shen and Jinnan Wu for their assistance in sampling during the KECES cruise. The KECES cruise was organized by the State Key Laboratory of Marine Geology, Tongji University, and funded by the National Key R&D Program of China (No. 2022YFF0800504), National Natural Science Foundation of China (Grant Nos. 41991324, 4173053, 42376170). Jeffrey Paulo H. Perez acknowledges the GFZ Discovery Fund for his research fellowship. Chenyu Wang also thanks the Freie Universität Berlin-China Scholarship Council (FUB-CSC) PhD Program for her scholarship in Germany. We are grateful for the three reviewers for their extensive and very constructive insights that helped to clarify many important points in this paper.

Appendix A. Supplementary material

The supplementary material contains: 1) Calculation of a three endmember model; 2) Table S1 providing information about the three endmembers; 3) Table S2 presenting ^{9}Be and major elemental concentrations in sequentially extracted fractions of the SPM; 4) Table S3 presenting specific surface area data and the surface area normalized ^{9}Be concentration in the exchangeable fraction; 5) Table S4 showing the results of calculated $\Delta[^{9}Be]_{diss}$ and Δ[DIP], and 6) the Powder X-ray diffraction (XRD) pattern of selected SPM samples with representative salinity. Supplementary material to this article can be found online at https://doi.org/10.1016/j.gca.2024.01.029.

References

Aldahan, A., Haiping, Y., Possnert, G., 1999. Distribution of beryllium between solution and minerals (biotite and albite) under atmospheric conditions and variable pH. Chem. Geol. 156 (1), 209–229.
Andersson, P.S., Porcelli, D., Gustafsson, Ö., Ingri, J., Wasserburg, G.J., 2001. The importance of colloids for the behavior of uranium isotopes in the low-salinity zone of a stable estuary. Geochim. Cosmochim. Acta 65 (1), 13–25.
Audry, S., Blanc, G., Schäfer, J., Chaillou, G., Robert, S., 2006. Early diagenesis of trace metals (Cd, Cu Co, Ni, U, Mo, and V) in the freshwater reaches of a macrotidal estuary. Geochim. Cosmochim. Acta 70 (9), 2264–2282.
Boschi, V., Willenbring, J.K., 2016. The effect of pH, organic ligand chemistry and mineralogy on the sorption of beryllium over time. Environ. Chem. 13 (4), 711–722.
Boschi, V., Willenbring, J.K., 2021. Chemical and physical drivers of beryllium retention in two soil endmembers. Sci. Total Environ. 754, 141591.
Boyle, E.A., Edmond, J.M., Sholkovitz, E.R., 1977. The mechanism of iron removal in estuaries. Geochim. Cosmochim. Acta 41 (9), 1313–1324.
Brown, E.T., Measures, C.I., Edmond, J.M., Bourlès, D.L., Raisbeck, G.M., Yiou, F., 1992. Continental inputs of beryllium to the oceans. Earth Planet. Sci. Lett. 114 (1), 101–111.
Brunauer, S., Emmett, P.H., Teller, E., 1938. Adsorption of gases in multimolecular layers. J. Amer. Chem. Sot. 60, 309–319.
Burnett, W.C., Taniguchi, M., Oberdorfer, J., 2001. Measurement and significance of the direct discharge of groundwater into the coastal zone. J. Sea Res. 46 (2), 109–116.
Cao, Z., Rao, X., Yu, Y., Siebert, C., Hathorne, E.C., Liu, B., Wang, G., Lian, E., Wang, Z., Zhang, R., Gao, L., Wei, G., Yang, S., Dai, M., Frank, M., 2021. Stable barium isotope dynamics during estuarine mixing. Geophys. Res. Lett. 48 (19).
Carpenter, J.H., 1965. The Chesapeake Bay institute technique for the Winkler dissolved oxygen method. Limnol. Oceanogr. 10 (1), 141–143.
Chetelat, B., et al., 2008. Geochemistry of the dissolved load of the Changjiang Basin rivers: anthropogenic impacts and chemical weathering. Geochim. Cosmochim. Acta 72 (17), 4254–4277.
Coffey, M., Dehairs, F., Collette, O., Luther, G., Church, T., Jickells, T., 1997. The behaviour of dissolved barium in estuaries. Estuar. Coast. Shelf Sci. 45 (1), 113–121.
Dannhaus, N., Wittmann, H., Krám, P., Christl, M., von Blanckenburg, F., 2018. Catchment-wide weathering and erosion rates of mafic, ultramafic, and granitic rock from cosmogenic meteoric ^{10}Be/^{9}Be ratios. Geochim. Cosmochim. Acta 222, 618–641.
de Bruin, H., Fardy, J., Temple, R., 1963. The ion-exchange behaviour of beryllium Salicylate Complexes. Aust. J. Chem. 16 (3), 376–391.
Deng, K., et al., 2023. Dominance of benthic fluxes in the oceanic beryllium budget and implications for paleo-denudation records. Sci. Adv. 9 (23), eadg3702.
Deng, K., Yang, S., Du, J., Lian, E., Vance, D., 2022. Dominance of benthic flux of REEs on continental shelves: implications for oceanic budgets. Geochem. Perspect. Lett. 22, 26–30.
Diaz, R.J., Rosenberg, R., 2008. Spreading dead zones and consequences for marine ecosystems. Science 321 (5891), 926–929.
Gagan, M.K., et al., 2002. Coral oxygen isotope evidence for recent groundwater fluxes to the Australian Great Barrier Reef. Geophys. Res. Lett. 29 (20), 43-1-43-4.

Guo, X., Xu, B., Burnett, W.C., Wei, Q., Nan, H., Zhao, S., Charette, M.A., Lian, E., Chen, G., Yu, Z., 2020. Does submarine groundwater discharge contribute to summer hypoxia in the Changjiang (Yangtze) River Estuary? Sci. Total Environ. 719, 137450.
Homoky, W.B., Weber, T., Berelson, W.M., Conway, T.M., Henderson, G.M., van Hulten, M., Jeandel, C., Severmann, S., Tagliabue, A., 2016. Quantifying trace element and isotope fluxes at the ocean–sediment boundary: a review. Philos. Trans. Roy. Soc. A: Math. Phys. Eng. Sci. 374 (2081).
Jiang, S., Ibánhez, J.S.P., Wu, Y., Zhang, J., 2021. Geochemical tracers in submarine groundwater discharge research: practice and challenges from a view of climate changes. Environ. Rev. 29 (2), 242–259.
Jiang, X., Lu, B., He, Y., 2013. Response of the turbidity maximum zone to fluctuations in sediment discharge from river to estuary in the Changjiang Estuary (China). Estuar. Coast. Shelf Sci. 131, 24–30.
Kim, I., Kim, G., 2014. Submarine groundwater discharge as a main source of rare earth elements in coastal waters. Mar. Chem. 160, 11–17.
Kong, W., Zhou, L., Aumaître, G., Bourlès, D., Keddadouche, K., 2021. Dissolved and particulate beryllium isotopes in the Pearl River Estuary: their geochemical behavior in estuarine water and potential contributions from anthropogenic sources. Front. Mar. Sci. 8.
Kusakabe, M., Ku, T.-L., Southon, J.R., Measures, C.I., 1990. Beryllium isotopes in the ocean. Geochem. J. 24, 263–272.
Kusakabe, M., Ku, T.L., Southon, J.R., Shao, L., Vogel, J.S., Nelson, D.E., Nakaya, S., Cusimano, G.L., 1991. Be isotopes in rivers/estuaries and their oceanic budgets. Earth Planet. Sci. Lett. 102 (3–4), 265–276.
Li, Y.-H., Burkhardt, L., Buchholtz, M., O'Hara, P., Santschi, P.H., 1984a. Partition of radiotracers between suspended particles and seawater. Geochim. Cosmochim. Acta 48 (10), 2011–2019.
Li, Y.-H., Burkhardt, L., Teraoka, H., 1984b. Desorption and coagulation of trace elements during estuarine mixing. Geochim. Cosmochim. Acta 48 (10), 1879–1884.
Li, J., Zhang, C., 1998. Sediment resuspension and implications for turbidity maximum in the Changjiang Estuary. Mar. Geol. 148 (3), 117–124.
Li, L., Zhong, Q., Du, J., 2021. Radium desorption behavior of riverine suspended sediment: Theoretical and experimental. J. Environ. Radioact. 234, 106644.
Lian, E., Yang, S., Wu, H., Yang, C., Li, C., Liu, J.T., 2016. Kuroshio subsurface water feeds the wintertime Taiwan Warm Current on the inner East China Sea shelf. J. Geophys. Res. Ocean. 121 (7), 4790–4803.
Lin, J., He, Q., Guo, L., van Prooijen, B.C., Wang, Z.B., 2020. An integrated optic and acoustic (IOA) approach for measuring suspended sediment concentration in highly turbid environments. Mar. Geol. 421.
Liu, J., Krom, M.D., Ran, X., Zang, J., Liu, J., Yao, Q., Yu, Z., 2020. Sedimentary phosphorus cycling and budget in the seasonally hypoxic coastal area of Changjiang Estuary. Sci. Total Environ. 713, 136389.
Liu, Q., Zhang, J., He, H., Ma, L., Li, H., Zhu, S., Matsuno, T., 2022. Significance of nutrients in oxygen-depleted bottom waters via various origins on the mid-outer shelf of the East China Sea during summer. Sci. Total Environ. 826, 154083.
Lohan, M.C., Bruland, K.W., 2008. Elevated Fe(II) and dissolved Fe in hypoxic shelf waters off Oregon and Washington: an enhanced source of iron to coastal upwelling regimes. Environ. Sci. Technol. 42 (17), 6462–6468.
Mallick, D., Wang, X., Beebe, D.A., 2022. Impact of estuaries on fluvial Cr input into the ocean: perspectives from the Mobile Bay Estuary, Northern Gulf of Mexico. Geochim. Cosmochim. Acta. 334, 187–200.
Measures, C.I., Edmond, J.M., 1983. The geochemical cycle of ^{9}Be: a reconnaissance. Earth Planet. Sci. Lett. 66 (66), 101–110.
Merschel, G., Bau, M., Dantas, E.L., 2017. Contrasting impact of organic and inorganic nanoparticles and colloids on the behavior of particle-reactive elements in tropical estuaries: an experimental study. Geochim. Cosmochim. Acta 197, 1–13.
Millero, F.J., Sotolongo, S., Izaguirre, M., 1987. The oxidation kinetics of Fe(II) in seawater. Geochim. Cosmochim. Acta 51 (4), 793–801.
Milliman, J.D., Farnsworth, K.L., 2011. In: River discharge to the coastal ocean – A global synthesis. Cambridge Univ Press, p. 392.
Moore, W.S., 1996. Large groundwater inputs to coastal waters revealed by ^{226}Ra enrichments. Nature 380 (6575), 612–614.
Mosley, L.M., Liss, P.S., 2020. Particle aggregation, pH changes and metal behaviour during estuarine mixing: review and integration. Mar. Freshw. Res. 71 (3).
Óvári, M., Csukás, M., Záray, G., 2001. Speciation of beryllium, nickel, and vanadium in soil samples from Csepel Island. Hungary. Fresenius J. Anal. Chem. 370 (6), 768–775.
Renner, R.M., 1989. On the resolution of compositional datasets into convex combinations of extreme vectors. Ph.D. thesis, Victoria University of Wellington, Wellington.
Rhee, H.H., Seong, Y.B., Lee, M.K., Jeong, A., Dash, C., Lee, J.I., Yoo, K.-C., Yu, B.Y., 2022. Spatial variations of authigenic beryllium isotopes in surface sediments of the Antarctic oceans: a proxy for sea ice dynamics and sedimentary environments. Geosci. J. 26 (4), 455–467.
Rousseau, T.C., Sonke, J.E., Chmeleff, J., van Beek, P., Souhaut, M., Boaventura, G., Seyler, P., Jeandel, C., 2015. Rapid neodymium release to marine waters from lithogenic sediments in the Amazon estuary. Nat. Commun. 6, 7592.
Ryan, J.G., 2002. Trace-element systematics of beryllium in terrestrial materials. Rev. Mineral. Geochem. 50 (1), 121–145.
Samanta, S., Dalai, T.K., 2016. Dissolved and particulate Barium in the Ganga (Hooghly) River estuary, India: Solute-particle interactions and the enhanced dissolved flux to the oceans. Geochim. Cosmochim. Acta 195, 1–28.
Shi, X., Wei, L., Hong, Q., Liu, L., Wang, Y., Shi, X., Ye, Y., Cai, P., 2019. Large benthic fluxes of dissolved iron in China coastal seas revealed by ^{224}Ra/^{228}Th disequilibria. Geochim. Cosmochim. Acta 260, 49–61.
Sholkovitz, E., Szymczak, R., 2000. The estuarine chemistry of rare earth elements: comparison of the Amazon, Fly, Sepik and the Gulf of Papua systems. Earth Planet. Sci. Lett. 179 (2), 299–309.
Shravanraj, K., Rejith, R.G., Sundararajan, M., 2021. Evaluation of heavy metals in coastal aquifers and seawater: an appraisal of geochemistry using ICPMS and remote sensing. Remote Sens. Ocean Coast. Environ 155–176.
Sproson, A.D., Yokoyama, Y., Miyairi, Y., Aze, T., Totten, R.L., 2022. Holocene melting of the West Antarctic Ice Sheet driven by tropical Pacific warming. Nat. Commun. 13 (1), 2434.
Suhrhoff, T.J., Rickli, J., Crocket, K., Bura-Nakic, E., Vance, D., 2019. Behavior of beryllium in the weathering environment and its delivery to the ocean. Geochim. Cosmochim. Acta 265, 48–68.
Sunda, W.G., 2012. Feedback interactions between trace metal nutrients and phytoplankton in the ocean. Front. Microbiol. 3, 204.
Sunda, W.G., Huntsman, S.A., 1987. Microbial oxidation of manganese in a North Carolina estuary. Limnol. Oceanogr. 32 (3), 552–564.
Tipper, E.T., Stevenson, E.I., Alcock, V., Knight, A.C.G., Baronas, J.J., Hilton, R.G., Bickle, M.J., Larkin, C.S., Feng, L., Relph, K.E., Hughes, G., 2021. Global silicate weathering flux overestimated because of sediment-water cation exchange. P. Natl. Acad. Sci. USA 118 (1).
Tomczak, M., 1981. A multi-parameter extension of temperature/salinity diagram techniques for the analysis of non-isopycnal mixing. Prog. Oceanogr. 10 (3), 147–171.
Vaquer-Sunyer, R., Duarte, C.M., 2008. Thresholds of hypoxia for marine biodiversity. P. Natl. Acad. Sci. USA 105 (40), 15452–15457.
Vesely, J., Norton, S.A., Skrivan, P., Majer, V., Kram, P., Navratil, T., Kaste, J.M., 2002. Environmental chemistry of beryllium. Rev. Mineral. Geochem. 50 (1), 291–317.
von Blanckenburg, F., Bouchez, J., 2014. River fluxes to the sea from the ocean's ^{10}Be/^{9}Be ratio. Earth Planet. Sci. Lett. 387, 34–43.
von Blanckenburg, F., O'Nions, R.K., Belshaw, N.S., Gibb, A., Hein, J.R., 1996. Global distribution of beryllium isotopes in deep ocean water as derived from Fe-Mn crusts. Earth Planet. Sci. Lett. 141 (1), 213–226.
von Blanckenburg, F., Bouchez, J., Ibarra, D.E., Maher, K., 2015. Stable runoff and weathering fluxes into the oceans over Quaternary climate cycles. Nat. Geosci. 8 (7), 538–542.
von Blanckenburg, F., Wittmann, H., Schuessler, J.A., 2016. HELGES: Helmholtz Laboratory for the Geochemistry of the Earth Surface. J. Large-scale Res. Facilit. 2.
von Blanckenburg, F., Bouchez, J., Willenbring, J.K., Ibarra, D.E., Rugenstein, J.K.C., 2022. There is no Neogene denudation conundrum. P. Natl. Acad. Sci. USA 119 (35), e2202387119.
Wang, X., Baskaran, M., Su, K., Du, J., 2018. The important role of submarine groundwater discharge (SGD) to derive nutrient fluxes into River dominated Ocean Margins – The East China Sea. Mar. Chem. 204, 121–132.
Wang, C., Frick, D.A., von Blanckenburg, F., Frank, M., Lian, E., Yang, S., Wittmann, H., 2024. Simultaneous preconcentration of 9Be and cosmogenic 10Be for determination of the 10Be/9Be ratio in (coastal) seawater. Limnol. Oceanogr. Methods 22, 14–24.
Wang, Z.-L., Liu, C.-Q., 2003. Distribution and partition behavior of heavy metals between dissolved and acid-soluble fractions along a salinity gradient in the Changjiang Estuary, eastern China. Chem. Geol. 202 (3–4), 383–396.
Wang, Z.-L., Liu, C.-Q., 2008. Geochemistry of rare earth elements in the dissolved, acid-soluble and residual phases in surface waters of the Changjiang Estuary. J. Oceanogr. 64 (3), 407–416.
Wang, X., Wu, Y., Wu, H., Zhang, G., Jin, J., Qi, L., Guo, X., Dai, J., Zhang, Z., Zhou, M., 2021. Organic carbon production and nutrients consumption revealed by mixing model in the energetic Changjiang Estuary. Estuar. Coast. Shelf Sci. 260, 107491.
White, D.A., Fink, D., Post, A.L., Simon, K., Galton-Fenzi, B., Foster, S., Fujioka, T., Jeromson, M.R., Blaxell, M., Yokoyama, Y., 2019. Beryllium isotope signatures of ice shelves and sub-ice shelf circulation. Earth Planet. Sci. Lett. 505, 86–95.
Willenbring, J.K., von Blanckenburg, F., 2010. Long-term stability of global erosion rates and weathering during late-Cenozoic cooling. Nature 465 (7295), 211–214.
Wittmann, H., von Blanckenburg, F., Bouchez, J., Dannhaus, N., Naumann, R., Christl, M., Gaillardet, J., 2012. The dependence of meteoric ^{10}Be concentrations on particle size in Amazon River bed sediment and the extraction of reactive ^{10}Be/^{9}Be ratios. Chem. Geol. 318, 126–138.
Wittmann, H., von Blanckenburg, F., Mohtadi, M., Christl, M., Bernhardt, A., 2017. The competition between coastal trace metal fluxes and oceanic mixing from the ^{10}Be/^{9}Be ratio: Implications for sedimentary records. Geophys. Res. Lett. 44 (16), 8443–8452.
Wu, J., Liu, J.T., Wang, X., 2012. Sediment trapping of turbidity maxima in the Changjiang Estuary. Mar. Geol. 303–306, 14–25.
Xu, J., Zhou, P., Lian, E., Wu, H., Liu, D., 2021. Spatial distribution of chlorophyll a and its relationships with environmental factors influenced by front in the Changjiang River Estuary and its adjacent waters in summer 2019. Mar. Sci. Bull. 40, 541–549.
Xu, X., 1994. Geochemical studies of beryllium isotopes in marine and continental natural systems. Ph.D. thesis. Univ. Southern California.
Yang, C., Vigier, N., Lian, E., Lai, Z., Yang, S., 2021. Decoupling of dissolved and particulate Li isotopes during estuarine processes. Geochem. Perspect. Lett. 40–44.
You, C.F., Lee, T., Li, Y.H., 1989. The partition of Be between soil and water. Chem. Geol. 77 (2), 105–118.

Zhang, Q., Liu, H., Qin, S., Yang, D., Liu, Z., 2014. The study on seasonal characteristics of water masses in the western East China Sea shelf area. Acta Oceanol. Sin. 33 (11), 64–74.

Zhao, X., Su, Y., Lei, Z., Wang, H., Hu, E., Hu, F., Wang, Q., Xu, L., Fan, S., Liu, X., Hao, X., 2022. Adsorptive removal of beryllium by Fe-modified activated carbon prepared from lotus leaf. Environ. Sci. Pollut. Res. 30 (7), 18340–18353.

Zhu, J., Zhu, Z., Lin, J., Wu, H., Zhang, J., 2016. Distribution of hypoxia and pycnocline off the Changjiang Estuary, China. J. Mar. Syst. 154, 28–40.